Available online at www.sciencedirect.com
ScienceDirect
International Journal of Heat and Mass Transfer 50 (2007) 1075–1086
International Journal of HEAT and MASS TRANSFER
www.elsevier.com/locate/ijhmt

Experimental investigation on natural convection in horizontal channels with the upper wall at uniform heat flux

O. Manca, S. Nardini *

Dipartimento di Ingegneria Aerospaziale e Meccanica, Seconda Università degli Studi di Napoli, via Roma 29, 81031 Aversa (CE), Italy

Received 10 June 2005
Available online 13 November 2006

Abstract

An experimental investigation on natural convection of air in horizontal channels with well-insulated lower wall and a heated upper wall is carried out.

Flow visualization and air temperature measurements are employed to obtain a phenomenological description of air natural convection inside a horizontal, open-ended cavity with a heated upper plate and an unheated lower one.

A laminar flow, with a *C-loop* shape, is observed inside the open-ended cavity. The penetration length is dependent upon the Grashof number. The penetration length increases particularly by increasing either the distance between the walls or the heat flux. The temperature measurements confirm the flow visualization observations. The air temperature profiles inside the open ended cavity indicate that the temperature gradients along the gap cavity are weak for low heat fluxes values. Scale analysis is carried out and shows that penetration length depends on $Ra^{1/2}$, in accordance with other authors. Furthermore, the estimation of the penetration length depends on the values of the thickness of the boundary layer, evaluated in terms of distance between the walls. Monomial correlations for average Nusselt numbers and dimensionless wall temperatures are proposed in a range of Rayleigh number from 2.78×10^3 to 3.90×10^5 and for an aspect ratio between $2L/b = 10$ and $2L/b = 20$. The equations agree highly with the experimental results.

Keywords: Natural convection; Horizontal channel; Experimental investigation; Visualization

1. Introduction

The configuration of two horizontal heated walls has many technological applications such as electronic cooling, solar cells and chemical vapor deposition systems (CVD). A deep investigation of natural convection is required for some basic configurations, i.e. *open-ended cavity*. Following the suggestions of Vafai and Ettefagh [1], a cavity is called *open* if the horizontal parallel plates have a finite extension and there is only one vertical permeable surface, whereas a cavity is called *open-ended cavity* if the permeable surfaces are two vertical parallel surfaces. They emphasized that although the two configurations share a similar geometry, due to the symmetry, the boundary conditions and the physical conditions are quite different.

The open cavities were widely investigated both experimentally and numerically [2–4]. Bejan and Kimura [5] carried out one of the first investigations about this topic. The authors investigated the natural convection in a horizontal cavity linked to a large external reservoir both analytically and experimentally. They showed that the flow is made of a recirculative pattern along the horizontal direction. This penetration length was found to be proportional to the height of the cavity and to the square root of the Rayleigh number. They validated their findings with an experimental analysis carried out by means of flow visualization. Numerical investigations of natural convection in isothermal open square cavities were reported in [6,7]. In the first paper the effects of cavity inclination, aspect ratio, wall temperature

---

* Corresponding author. Tel.: +39 081 5010347; fax: +39 081 5010204.
E-mail address: sergio.nardini@unina2.it (S. Nardini).

0017-9310/$ - see front matter © 2006 Elsevier Ltd. All rights reserved.
doi:10.1016/j.ijheatmasstransfer.2006.07.038

Nomenclature

b	channel spacing, m
g	acceleration of gravity, m s^{-2}
Gr	Grashof number, Eq. (1), dimensionless
h	heat transfer coefficient, W m^{-2} K^{-1}
k	thermal conductivity, W m^{-1} K^{-1}
l_p	penetration length, m
L	half length of the plate, m
Nu	average Nusselt number, dimensionless
p	pressure, Pa
q	heat flux, W/m^2
Ra	$= Gr\,Pr$ Rayleigh number, dimensionless
T	temperature, K
T^+	dimensionless temperature, Eq. (2)
x	coordinate along the length of the plates, m
u	velocity component along x, m s^{-1}
v	velocity component along y, m s^{-1}
y	coordinate along the channel spacing, m
z	coordinate along the width of the plates, m
W	width of the plate, m

Greek symbols

α	thermal diffusivity, m^2 s^{-1}
β	volumetric coefficient of expansion, K^{-1}
δ	boundary layer thickness, m
ρ	density, kg m^{-3}
ν	kinematic viscosity, m^2 s^{-1}

Subscripts

c	convective
k	conductive
l	lower
o	ambient air
r	radiative, reference
u	upper
w	wall
δ	referred to boundary layer thickness
Ω	Ohmic dissipation

and Grashof number were studied, taking into account the temperature dependent properties. In the second investigation the effects of inclination and Grashof number were carried out and the results showed two kinds of unsteady motions inside the cavity. In an experimental study, Hess and Henze [8] investigated natural convection inside a horizontal open cavity. In the cavity the upper and lower surfaces were unheated and the vertical wall opposite the open vertical surface was isothermal.

A numerical study of two-dimensional, natural convection in open square cavities, with isothermal vertical wall and adiabatic horizontal walls was conducted by Chan and Tien [9]. Results showed that, for Rayleigh numbers ranging from 10^3 to 10^9, solutions approached those for natural convection over a vertical plate. Numerical and experimental investigations on shallow rectangular open cavity were carried out in [10,11]. Results of a numerical study were obtained in [11] for two-dimensional, steady-state and laminar flow, for Rayleigh number up to 10^6. In the experimental investigation water was used as working fluid. Abib and Jaluria [12] investigated the *penetrative convection* induced by a heat source located on the lower surface of an open cavity. An open cavity, which was inclined forward the horizontal direction, was investigated by Elsayed and Chakroun [3]. Experiments was carried out for Grashof number equal to 5.5×10^8, different cavity openings and inclination angles. The numerical simulation of the laminar natural convection inside an open cavity, with an isothermally heated back wall, was carried out by Elsayed et al. [4]. The other walls were considered as adiabatic and the fluid was air. The solutions were given for Grashof numbers in the 10^2–10^5 range and angles between $-60°$ and $+90°$.

Numerical and experimental studies have also been carried out for open-ended cavities. For this configuration, the effects of the sharp corners and of the boundary conditions imposed at infinity on the vortex generation and flow instability were investigated by Vafai and Ettefagh [1]. At higher Rayleigh numbers, Vafai and Ettefagh [13] showed that, a one-to-one relationship exists between the frequency of the periodic oscillations in the Nusselt number, the central vortex's oscillations and the location inside the cavity. In air in this configuration experimental investigations on natural convection with lower and upper walls at uniform heat flux were conducted in [14,15]. In these papers, a flow visualization inside the open-ended cavity was carried out. In the case with heated upper surface and unheated lower one, a laminar penetrating flow in the cavity, with a *C-loop* shape, was observed, as also shown in the results given in [5]. A numerical study was carried out for air laminar flow by Andreozzi et al. [16] for the case with heated upper surface and unheated lower one.

Khanafer and Vafai [17] proposed a numerical analysis on natural convection in open-ended cavities for the reduction or elimination of the extended domain for two and three dimensional geometries. A numerical investigation on accurate representation of the effective boundary conditions at the open section of two-dimensional open-ended configurations for wide range of significant parameters was achieved in [18]. Baskaya and Kauli [19] accomplished a numerical study on steady state natural convection between asymmetrically heated horizontal parallel plates. A transient numerical analysis for laminar natural convection in air between two horizontal parallel plates, with the upper plate heated at uniform heat flux and the lower one unheated, was carried out in [20]. Two-dimensional natural

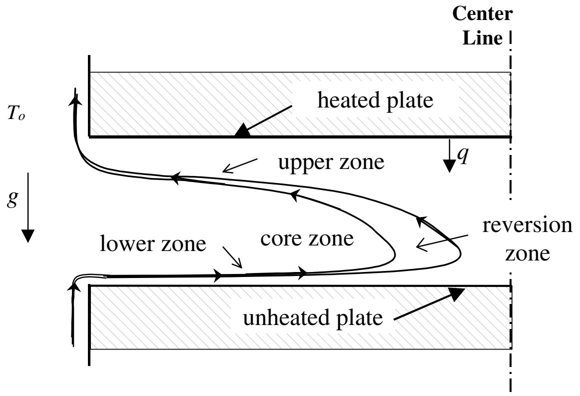

Fig. 1. Sketch of the flow pattern in open ended cavity with heated upper plate and unheated lower plate.

convection from localized heat sources in horizontal channel was studied numerically in [21]. In the analysis, heat transfer in air from two identical and isothermal protruding heat sources located at the lower surface of a horizontal channel was investigated.

The lack of in-depth investigations on open-ended cavities, heated with uniform heat flux, convinced the authors to delve into the phenomenological aspects of the configuration with heated upper plate and unheated lower one. This geometry is important in electronic cooling [21], in chemical vapor deposition processes [22] and in the study of smoke spread in building fire [12]. The analyzed open-ended cavity is made of two horizontal plates, with a gap distance equal to b, and opened to the surroundings so as to allow a flow rate. The upper plate is heated with uniform heat flux q, Fig. 1. This heat flux determines a convective flow motion inside the cavity, as reported in Fig. 1. The fluid penetrates into the cavity flowing along the lower plate, then it reverses the motion close to the central region and it exits the cavity close to the upper plate. This motion is called *C-loop*.

In this paper, an experimental analysis for air natural convection between two horizontal parallel plates with the upper plate heated with uniform heat flux and the lower one unheated is carried out by means of a visualization technique and temperature measurements of the air flow. A scale analysis is carried out to estimate the penetration length. Correlations between Nusselt number and maximum dimensionless wall temperature in terms of Rayleigh number are proposed.

2. Experimental apparatus

The experimental test section was made of two principal horizontal walls and two vertical side walls. Each principal wall consisted of two 400 × 530 mm^2 sandwiched phenolic fiberboard plates. The side walls were made of Plexiglas rectangular rods, machined to an accuracy of ±0.03 mm. The plate spacing was measured to an accuracy of ±0.25 mm by a dial-gauge equipped caliper.

The cavity was 400 mm long and 475 mm wide and was open to the ambient along the edges of the dimensions $W \times b$, Fig. 2a. In this investigation only the upper wall was heated.

The upper wall was made of two plates. The plate facing the channel was 3.2 mm thick and its surface adjacent to the internal air was coated with a 35 μm thick nickel plated copper layer. The low emissivity of nickel (0.05) minimized radiation effects on heat transfer. The rear plate was 1.6 mm thick. Its back surface was coated with a 17.5 μm thick copper layer, which was the heater. It was an electrical resistance obtained by cutting the copper layer in a serpentine shape. Its runs were 19.6 mm wide with a gap of nearly 0.5 mm between each one, giving the heater a total length of 9.0 m. Its expected electrical resistance was 0.50 Ω. The upper wall was heated by passing a direct electrical current through the heater. In order to reduce conductive heat losses, a 150 mm polystyrene block was affixed to the rear face of each principal wall.

The narrow gaps between the runs, together with the relatively high thickness (4.8 mm) of the resulting low-conductive fiberglass were suitable to maintain a nearly uniform heat flux at the plate surface [23]. Direct electrical current through the heaters was accomplished by using a Hewlett–Packard 6260B d.c. power supply. The electrical power supplied was evaluated by measuring the voltage drop across the plate and the current passing through it. A HP-3465A digital multi-meter measured the voltage drop, while the current was calculated by the measured voltage drop across a reference resistance. To avoid electrical contact resistances, thick copper bars soldered both to the electric supply wire and to the ends of heater were

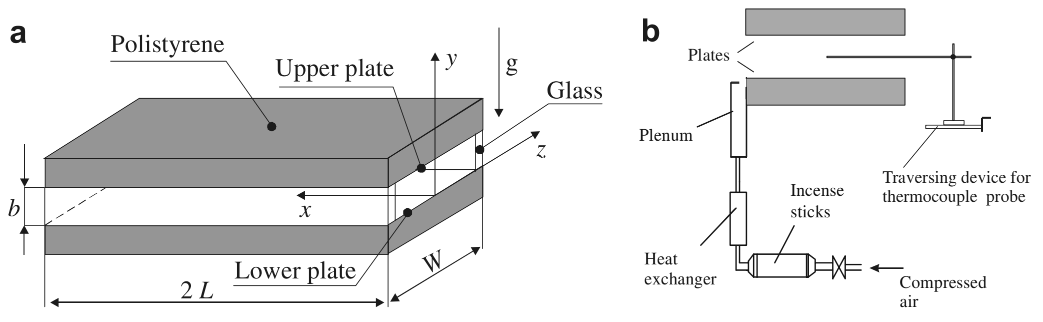

Fig. 2. (a) View of the test section; (b) sketch of the smoke generation arrangement.

bolted together. The dissipated heat flux was evaluated to an accuracy of ±2%. The entire apparatus was located within a room, sealed to eliminate extraneous air currents.

Wall temperatures were measured by thirty-six 0.50 mm OD ungrounded iron-constantan thermocouples embedded in each fiberboard plate and in contact with the outer layer. They were located at 12 longitudinal stations at three different z values. Fifteen thermocouples were affixed to the rear surface of the plates and embedded in the polystyrene to enable the evaluation of conductive heat losses.

The ambient air temperature was measured by a shielded thermocouple placed near the leading edge of the channel. A Kaye instrument K170 ice point was used as a reference for thermocouple junctions. Their voltages were recorded to 1 μV by a National Instruments SCXI module data acquisition system and a personal computer was used for the data collection and reduction. The acquired data were recorded and processed through the LabView™ 6.0 program. Calibration of the temperature measuring system showed an estimated precision of the thermocouple-readout system of ±0.1 °C.

The temperature of the air in the open-ended cavity was measured by one J-type OMEGA thermocouple with a sheath diameter of 0.25 mm and exposed junction. The wire diameter was 50 μm and the junction was considered a sphere with a diameter of about 125 μm. A response time of 0.20 s was estimated by considering a Nusselt number of 2.0 for the sphere [24]. The thermocouple was mounted on a very thin glass cylinder. The maximum time fluctuations were lower than ±0.1 °C and the maximum temperature differences along the z-axis were lower than 10% of the average value at the transversal section (y–z-plane). Thus, the thermal field was considered steady and two-dimensional.

The thermocouple was positioned inside the cavity using a micrometer traversing mechanism, Fig. 2b. It allowed positioning of the thermocouple along x and y axes to an accuracy of ±0.03 mm and along the z-coordinate to an accuracy ±0.1 mm.

Smoke for flow visualization was generated by burning incense sticks in a steel tube, connected to a compressor. The smoke was injected through a glass heat exchanger to reduce its temperature, which, measured by a thermocouple, turned out to be close to that of the ambient air entering the cavity. Finally, the smoke was passed into a plenum and driven to the test section through a small slot situated under the leading edge of the bottom plate along the plate width. A sketch, both of the test section and of the experimental apparatus is reported in Fig. 2. Particularly, the longitudinal view of the arrangement for the air temperature measurements and of the visualization set-up is shown in Fig. 2b. Preliminary tests were carried out to determine the plenum location that do not interfere with the air flow at the inlet section. The visualization was made possible by means of a laser sheet, generated by a He–Ne laser source. The laser sheet was produced by passing the laser beam through a cylindrical lens to enlarge the beam as needed, Fig. 3. Small adjustments were allowed by means of a micrometer screw system, in order to take photographs at different locations along the z-axis. The still camera was a programmable Nikon F90X and the film was a Kodak TMAX™ 3200.

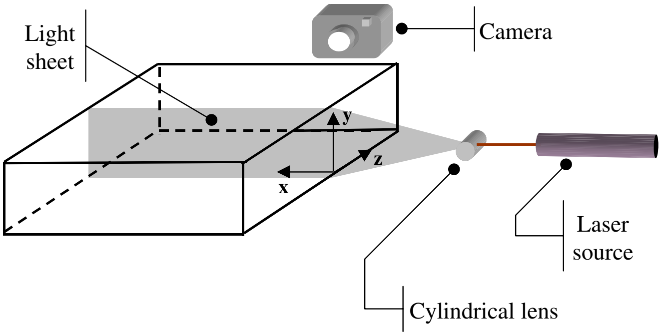

Fig. 3. Sketch of the visualization arrangement.

3. Data reduction

The Grashof number is defined as:

$$Gr = \frac{g\beta q_c b^4}{\nu^2 k} \tag{1}$$

and the dimensionless temperature is

$$T^+ = \frac{T - T_o}{2q_c b/k} \tag{2}$$

where q_c is the average convective heat flux:

$$q_c = \frac{1}{2}\frac{1}{2L}\left[\int_0^{2L} q_{c,l}(x)\,dx + \int_0^{2L} q_{c,u}(x)\,dx\right] \tag{3}$$

The thermophysical properties are evaluated at the reference temperature: $T_r = \frac{T_w + T_o}{2}$ with

$$T_w = \frac{1}{2}\frac{1}{2L}\left[\int_0^{2L} T_{w,l}(x)\,dx + \int_0^{2L} T_{w,u}(x)\,dx\right] \tag{4}$$

where $T_{w,l}(x)$ and $T_{w,u}(x)$ are the spanwise average values.

The Nusselt number is

$$Nu = \frac{hb}{k} = \frac{q_c}{T_w - T_o}\frac{b}{k} \tag{5}$$

Local convective heat flux, $q_c(x)$, was not uniform because of radiation and conduction heat losses. Experimental data were reduced by first introducing, in the equations presented above, the local convective heat flux

$$q_c(x) = q_\Omega(x) - q_k(x) - q_r(x) \tag{6}$$

where $q_\Omega(x)$ is the local heat flux due to Ohmic dissipation, assumed uniform along x, $q_k(x)$ the local conduction heat losses from the plate and $q_r(x)$ the local radiative heat flux from the plate. For each run, the terms $q_k(x)$ were calculated by means of a numerical procedure, a three-dimensional distribution of the temperature being assumed in the polystyrene. Therefore, q_k on the plate wall was a func-

Table 1
Percentage uncertainty values ($U_{X_i}/X_i 100$)

Variable	T_o	$T_w - T_o$	q_c	q_r	$q_c + q_r$	q_Ω	q_k	b
Uncertainty	0.068	4.0	5.7	5.0	2.5	2.0	4.2	1.3

tion of both x and z coordinates, and its values were averaged along z. The predicted temperatures for some configurations of the system were previously compared with those measured by thermocouples embedded in the polystyrene insulation and the harmony was very good, the maximum deviation being 3%. A two-dimensional radiative cavity was made of the two plates, considered as diffuse-gray surfaces and the two black edge sections at room temperature. In all cases the radiative heat losses were not greater than 2% of the Ohmic dissipated power. The $q_r(x)$ terms were calculated for each temperature distribution of the wall, ambient temperature and plate spacing, dividing each plate into 16 strips along its length.

3.1. Uncertainty analysis

The uncertainty of the *Gr* and *Nu* values was evaluated following the procedure suggested in [25,26]. Accordingly, the uncertainty of the dependent variable R as a function of the uncertainties of the independent variables X_i is given by the relation

$$U_R^2 = \left(\frac{\partial R}{\partial X_1} U_{X_1}\right)^2 + \left(\frac{\partial R}{\partial X_2} U_{X_2}\right)^2 + \cdots + \left(\frac{\partial R}{\partial X_j} U_{X_j}\right)^2 \tag{7}$$

Therefore, on the basis of Eqs. (1), (2), and (5) and of the non-negligible uncertainties of the values of the independent variables reported in Table 1, the uncertainty of the Grashof and the average Nusselt numbers were ±7% and ±4%, respectively.

4. Results and discussion

The air flow visualization inside the open-ended cavity is reported in Fig. 4 for an Ohmic wall heat flux of 60 W/m^2 and three plate gaps, $b = 20.0$, 32.3 and 40.0 mm and the corresponding Rayleigh numbers are 1.26×10^4, 8.74×10^4 and 2.00×10^5.

4.1. Flow visualization and air temperature

The photographs show that the greater b, i.e. *Ra*, the deeper the penetration of the fluid motion inside the open-ended cavity. It is observed that the flow penetrates up to about 140–150 mm for $b = 20.0$ mm and $Ra = 1.26 \times 10^4$, and the penetration length is $l_p \approx 7b$. This picture enforces what was sketched in Fig. 1b. In fact, the fluid enters through the inlet section close to the lower plate and flows over it with a boundary layer flow up to about $x = 60$ mm ($\approx 3b$). Then, the motion reversion takes place between $x \approx 3b$ and $7b$. This indicates a low velocity magnitude along y and a subsequent low heat transfer coefficient. Then the fluid goes toward the hot upper surface and exits the open-ended cavity from the upper region. The fluid motion is laminar along the two walls and in the reversion zone. As b increases, the flow enters up to half the length of the wall and when $b = 32.3$ mm ($Ra = 8.74 \times 10^4$), Fig. 4b, the reversion zone is more extended than in the case with $b = 40.0$ mm ($Ra = 2.00 \times 10^5$), Fig. 4c. This suggests greater velocities when $b = 40.0$ mm, and this is validated by the boundary layer thickness over the lower plate. Furthermore, a different *C-loop* shape is observed and also for these other configurations the fluid motion is laminar. It is noteworthy that the photos confirm the expected laminar fluid motion. For the assigned heat flux, the lower penetration length for the lower b value is due to greater interaction between the two flows, the one adjacent to the lower wall and the other one adjacent to the upper wall. Furthermore, the greater interaction and lower velocity determine a greater boundary layer thickness, which develops along the walls. The reversion zone is larger when the penetration is partial because the fluid flow can decelerate freely inside the cavity. If the penetration is complete, the two opposite fluid flows, which move along the lower wall, impact each other at the middle section and go toward the upper wall. In this case the reversion zone downsizes.

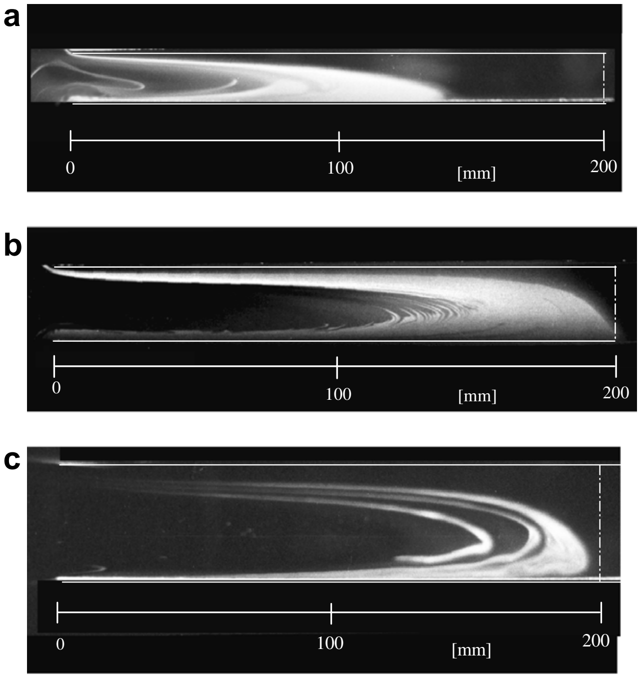

Fig. 4. Longitudinal section picture at $z = 0$ for $q_\Omega = 60$ W/m^2 and: (a) $b = 20.0$ mm, $Ra = 1.26 \times 10^4$, $L/b = 10$; (b) $b = 32.3$ mm, $Ra = 8.74 \times 10^4$, $L/b = 6.2$, (c) $b = 40.0$ mm, $Ra = 2.00 \times 10^5$, $L/b = 5$.

Air temperature rise respect to the ambient temperature as function of y-coordinate for several x-coordinates and as function of x-coordinate for several y-coordinates are reported in Figs. 5 and 6, respectively, for $q_\Omega = 60\ \mathrm{W/m^2}$ and $b = 20.0$, 32.3 and 40.0 mm ($Ra = 1.26 \times 10^4$, 8.74×10^4 and 2.00×10^5). For $b = 20.0$ mm ($Ra = 1.26 \times 10^4$), when $x \leqslant 60$ mm the temperature profiles in Fig. 5a show a steeper gradient in the upper region, close to the heated wall. Here, the heat transfer is more vigorous due to the fluid motion along the upper wall. For greater x, the temperature gradients along y, for different x values, are constant up to $y = 15$ mm, where the slope changes and is about 1.0×10^3 K/m. The *C-loop* penetrates up to about $x = 140$ mm, as observed in Fig. 4a, and the temperature profiles are almost linear for $x > 140$ mm. This indicates a nearly conductive field in the region between $140 < x < 200$.

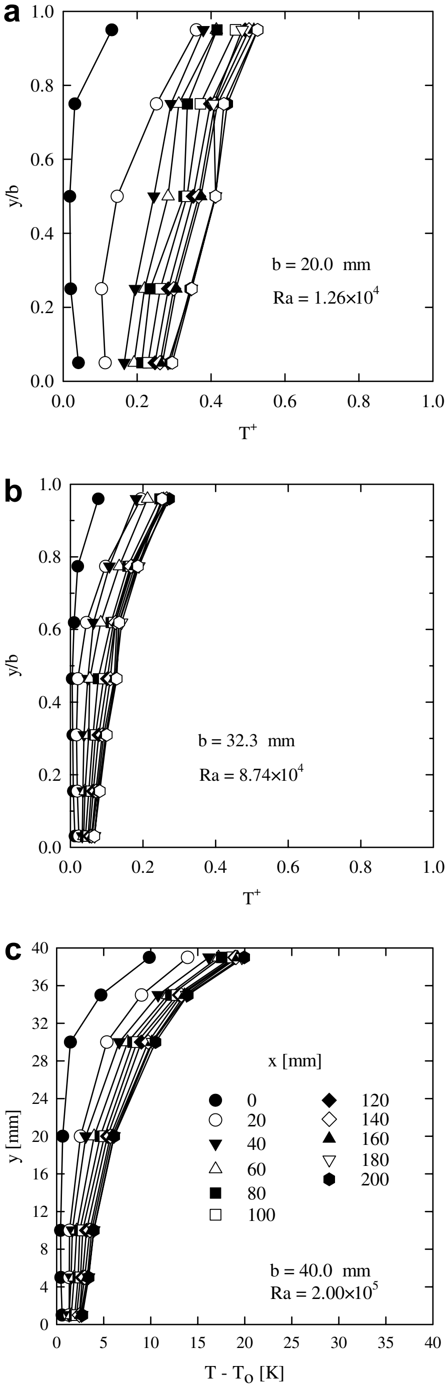

Fig. 5. Air temperature rise at $z = 0$ for $q_\Omega = 60\ \mathrm{W/m^2}$ as a function of y for: (a) $b = 20.0$ mm; (b) $b = 32.3$ mm; (c) $b = 40.0$ mm.

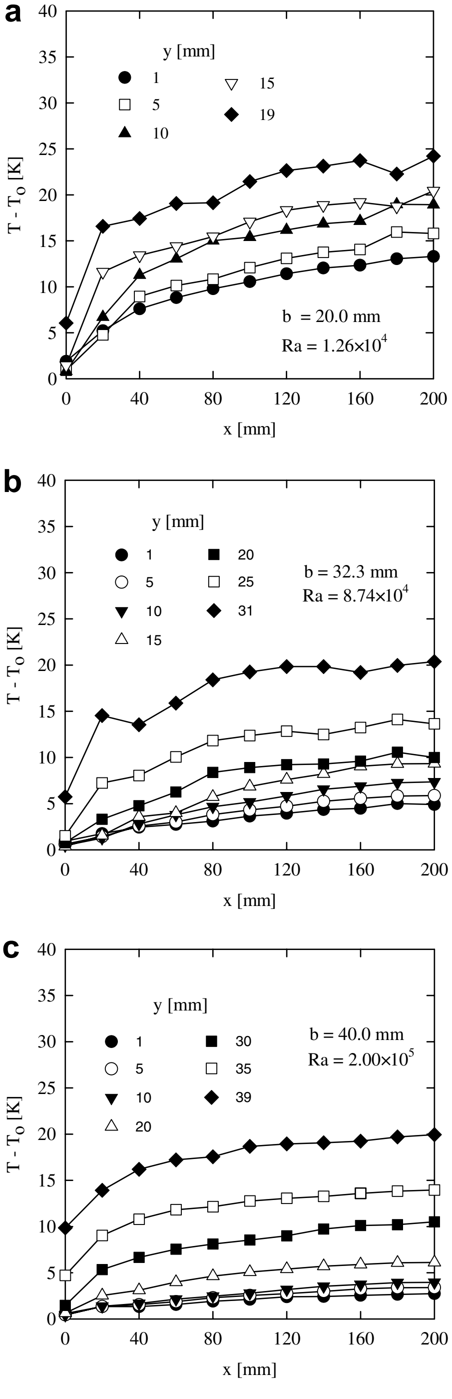

Fig. 6. Air temperature rise at $z = 0$ for $q_\Omega = 60\ \mathrm{W/m^2}$ as a function of x for: (a) $b = 20.0$ mm; (b) $b = 32.3$ mm; (c) $b = 40.0$ mm.

At $y = 1$ mm, Fig. 6a, the temperature increases almost regularly and with a parabola-like shape. As y increases the temperature slope increases along x just where the pictures present the motion reversion. This is because a more efficient heat transfer occurs for the fluid in the *C-loop*. In fact, the air entering from the environment flows along the lower unheated plate and reverses its motion meeting warmer regions. The fluid flows then toward the heated wall and than exits from the cavity from the upper region. The *C-loop* is more evident in the upper region due to the influence of the warm heated wall. A strong increment of the temperature is detected both when $y = 15$ mm and $y = 19$ mm going from $x = 0$ mm to that at $x = 20.0$ mm and this increase is about 10 °C.

The temperature profiles, when $b = 32.3$ mm ($Ra = 8.74 \times 10^4$), are shown in Figs. 5b and 6b. The first graph, Fig. 5b, shows that when the axial coordinate x is between 0 mm and 60 mm the profiles present a gradient along y, up to about $y = 15$ mm, almost negligible. The core region, up to about $x = 20.0$ mm, is the coldest one and, for $x > 60$ mm, the gradient along y increases as x, with the maximum value being 250 K/m. This happens up to about $y = 15$ mm. The thermal gradient along y increases with y for all the profiles, and reaches its maximum value on the plate, which is about 10×10^3 K/m. The temperature profiles along y confirm the complete penetration of the *C-loop* inside the cavity. Furthermore, the fluid temperature rise adjacent the lower wall is not greater than 5 °C in the considered points. Diffusive effects are weaker than in the previous case and the heat convection is the governing mechanism. The temperature profiles of the air inside the cavity as a function of the axial coordinate x, for fixed y-coordinate, are reported in Fig. 6b. The temperature increments are small up to $x \approx 10$ mm, and the reversion zone is located between $x = 140$ and $x = 200$ mm. The plots in Figs. 5c and 6c show the temperature profiles when $b = 40.0$ mm ($Ra = 2.00 \times 10^5$). These profiles show regular patterns along y with high gradients close to the upper heated wall, and very small close to the lower wall. The patterns are similar to the previous cases up to $y = 30$ mm. Temperature of the air adjacent the unheated wall is lower than in the previous case. This confirms the decrease of the diffusive effects when the distance between the walls increases. Fluid motion becomes freer and freer and heat transfer is mostly due to heat convection on the upper wall. Fluid flow penetrates up to the middle section moving over the lower wall with a rise in temperature not more than 3 °C in this zone. In the motion reversion zone, in accordance with Fig. 4c, for $x > 150$ mm, air temperature increases almost uniformly. In fact, this can be noticed also in Fig. 6c, where temperature varies a little, i.e. gradients along x for an assigned y value are small and certainly negligible with respect to the ones along y for an assigned x value. In addition, the thermal gradients increase constantly along y. The picture in Fig. 4c and the temperature profiles show a thermal and a fluid dynamic boundary layer thickness lower than the previous case, due also to the greater Grashof number. Furthermore, the temperature profiles along x present more regular patterns along the same direction compared to the previous cases.

The comparison between different configurations of the flow visualization along the longitudinal section is reported in Fig. 7 for $b = 32.3$ mm and three heat fluxes, $q_\Omega = 26$ W/m^2, 60 W/m^2 and 120 W/m^2 ($Ra = 3.52 \times 10^4$, 8.74×10^4 and 1.69×10^5). When $q_\Omega = 26$ W/m^2 ($Ra = 3.52 \times 10^4$), Fig. 7a, the flow penetration inside the cavity takes place up to about $x = 160$ mm ($\approx 5b$), and the fluid does not reach the transversal middle section of the cavity. In this case the reversion zone begins at about $x = 160$ mm ($\approx 5b$). On the contrary, for $q_\Omega = 60$ and 120 W/m^2 ($Ra = 8.74 \times 10^4$ and 1.69×10^5), Fig. 7b and c the fluid inside the *C-loop* penetrates up to the middle transversal section of the cavity. From an analysis of the photos it seems that the reversion zone begins at an x value slightly greater (about 140 mm) for $q_\Omega = 120$ W/m^2 than for $q_\Omega = 60$ W/m^2 where the reversion zone begins at about $x = 130$ mm. Finally, flow visualization shows a good agreement with streamlines fields given in [1,18], even if the configurations examined in these works had different boundary conditions, assigned temperature on lower and upper walls and higher than ambient temperature, and aspect ratio L/b lower than those studied in this work.

The temperature profiles as functions of y, for $b = 32.3$ mm and $q_\Omega = 26$, 60 and 120 W/m^2 ($Ra = 3.52 \times 10^4$, 8.74×10^4 and 1.69×10^5), are reported in Fig. 8. The temperature profiles along y show that, as the heat flux increases, the thermal gradients close to the upper heated plate also increase. For $q_\Omega = 26$ W/m^2 ($Ra = 3.52 \times 10^4$), Fig. 8a, in the core region of the cavity, the air temperature presents small modifications, while, when the heat flux increases, Fig. 8b and c, at $y = 25$ mm and $y = 31$ mm, the greatest temperature variations occur in the range $20.0 < x < 100$ mm. This is due to the strong thermal

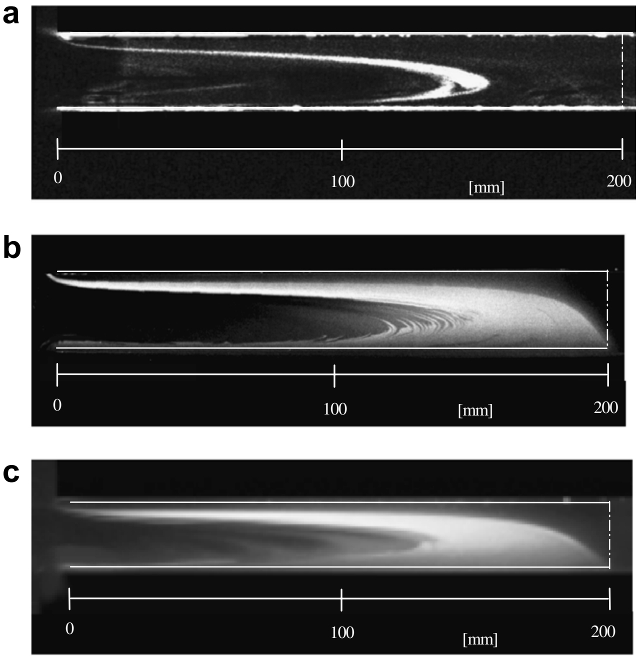

Fig. 7. Longitudinal section picture at $z = 0$ for $b = 32.3$ mm and: (a) $q_\Omega = 26$ W/m^2, $Ra = 3.52 \times 10^4$; (b) $q_\Omega = 60$ W/m^2, $Ra = 8.74 \times 10^4$; (c) $q_\Omega = 120$ W/m^2, $Ra = 1.69 \times 10^5$.

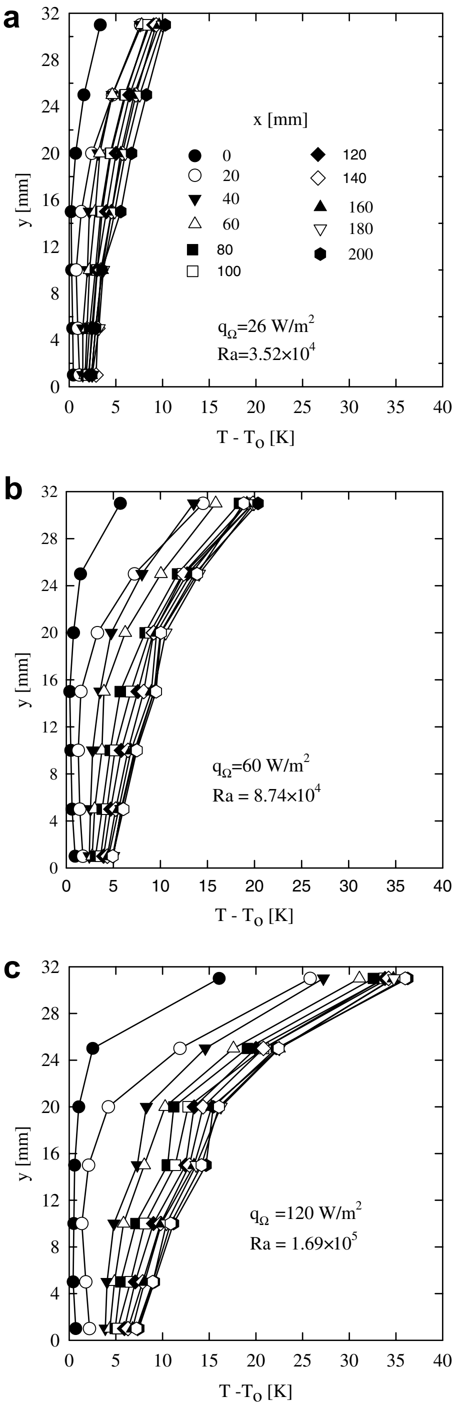

Fig. 8. Air temperature rise at $z = 0$ for $b = 32.3$ mm as a function of y for: (a) $q_\Omega = 26$ W/m^2, (b) $q_\Omega = 60$ W/m^2, (c) $q_\Omega = 120$ W/m^2.

gradients along y in the proximity of the heated plate. In fact, close to the heated wall, the difference between temperatures at $y = 31$ mm and at $y = 25$ mm is about 2 °C, for $q_\Omega = 26$ W/m^2, Fig. 8a, 6 °C for $q_\Omega = 60$ W/m^2, Fig. 8b, and 12 °C for $q_\Omega = 120$ W/m^2, Fig. 8c. At $y = 1$ mm the temperature increase along x is about 3 °C for $q_\Omega = 26$ W/m^2, in Fig. 8a, and 7 °C for 120 W/m^2, in Fig. 8c. For $q_\Omega = 26$ W/m^2, in Fig. 8a, temperature profile for $x \geqslant 120$ mm is almost linear for $y \geqslant 10$ mm and this could indicate that the heat transfer is due to mainly the diffusion. The *C-loop* does not penetrate completely inside the cavity. For $q_\Omega \geqslant 60$ W/m^2, Fig. 8b and c, temperature profiles confirm the complete penetration of the *C-loop* inside the cavity.

From temperature profile along the x-axis and different y values, in Fig. 9, it is noted that, for $q_\Omega = 26$ W/m^2 ($Ra = 3.52 \times 10^4$), in Fig. 9a, very close to the heated wall,

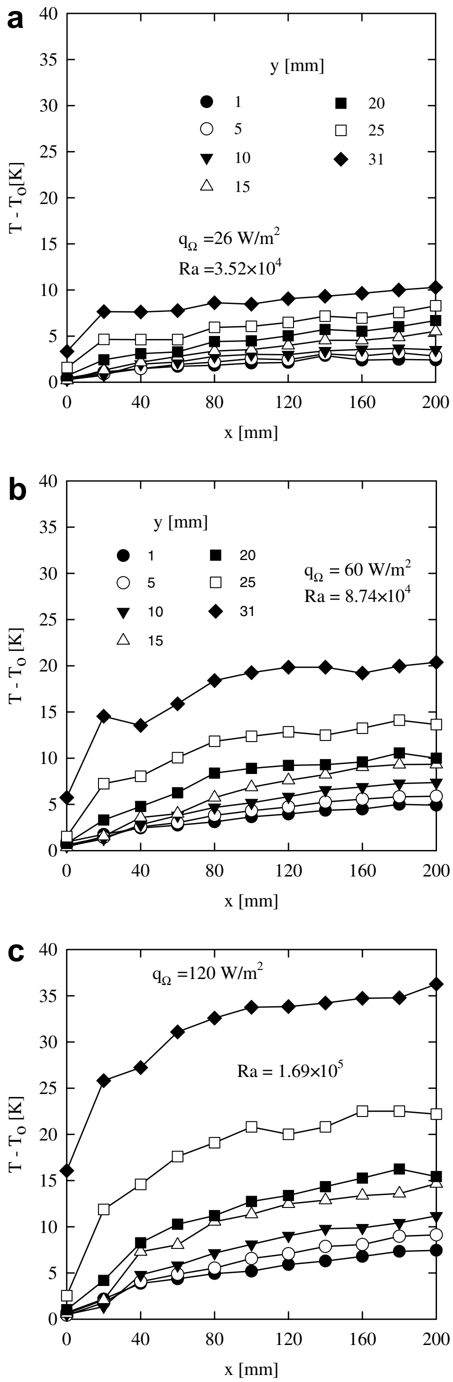

Fig. 9. Air temperature rise at $z = 0$ for $b = 32.3$ mm as a function of x for: (a) $q_\Omega = 26$ W/m^2, (b) $q_\Omega = 60$ W/m^2, (c) $q_\Omega = 120$ W/m^2.

$y = 31$ mm, decreasing the x value, temperature decreases almost linearly, whereas near the opening temperature decrease is greater. Also in the other two cases, in Fig. 9b and c ($Ra = 8.74 \times 10^4$ and 1.69×10^5), at $y = 31$ mm, air temperature decreases gradually from $x = 200$ mm to $x = 20$ mm, but the trend is different from the previous case in Fig. 9a. However, close to the opening section, a greater temperature decrease is observed. Moreover, temperature profiles confirm that the temperature gradients along y are larger close to the heated wall due to the fluid motion inside the cavity linked to the complete *C-loop* and diffusive effects inside the cavity are weak. In all cases, strong temperature variations in the region $x < 20.0$ mm close to the upper heated plate, $y \geqslant 25$ mm, are observed.

In order to give more general results, in Fig. 10, profiles of dimensionless temperature T^+, defined by Eq. (2), as function of y/b for several investigated configurations are presented. Particularly, profiles are reported for $Ra = 1.26 \times 10^4$, Fig. 10a ($b = 20.0$ mm, $q_\Omega = 60$ W/m^2), $Ra = 3.52 \times 10^4$, Fig. 10b ($b = 32.3$ mm, $q_\Omega = 26$ W/m^2), $Ra = 1.69 \times 10^5$, Fig. 10c ($b = 32.3$ mm, $q_\Omega = 120$ W/m^2) and $Ra = 2.00 \times 10^5$, Fig. 10d ($b = 40.0$ mm, $q_\Omega = 60$ W/m^2). It can be observed that when Rayleigh number increases, the dimensionless temperature inside the cavity decreases for the same y/b value. Profiles in the opening section are very similar to each other. This indicates that, in this section, there is fluid motion associated to the *C-loop*. Inside the cavity, for the lower Ra values dimensionless temperature profiles are nearly linear along y/b. This indicates a mostly diffusive heat transfer, as already observed from dimensional profiles. For the higher Ra values, the profiles are very similar and show the dominance of convective heat transfer associated to the fully penetrated *C-loop*. In addition, this effect determines the variation of the decrease of the dimensionless temperature when Ra rises. A comparison with numerical data given in [16] for the case in Fig. 10b shows that the numerical data are higher than the experimental ones. This is due to a lower Ra value in the experiments and the heat conduction inside the walls that in the numerical case is not considered.

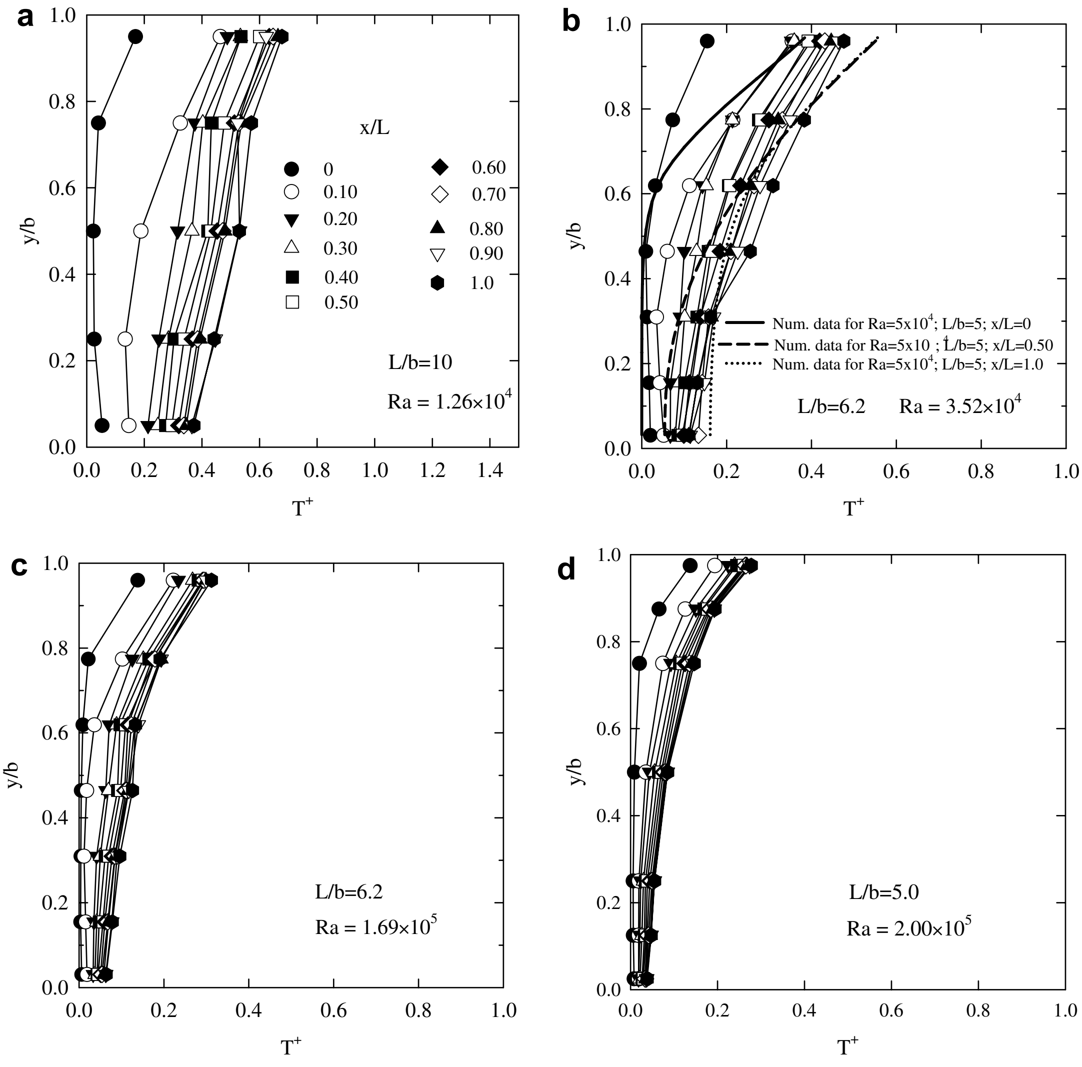

Fig. 10. Dimensionless air temperature rise as a function of y/b: (a) $Ra = 1.26 \times 10^4$; (b) $Ra = 3.52 \times 10^4$; (c) $Ra = 1.69 \times 10^5$; (d) $Ra = 2.00 \times 10^5$.

4.2. Scale analysis

The scale of lateral penetration length l_p of the *C-loop* inside the cavity can be determined by the governing equations of natural convection in two-dimensional, laminar steady state with thermophysical properties constant with temperature and with the Boussinesq approximation

$$\frac{\partial u}{\partial x}+\frac{\partial v}{\partial y}=0 \tag{8}$$

$$u\frac{\partial u}{\partial x}+v\frac{\partial u}{\partial y}=-\frac{1}{\rho}\frac{\partial p}{\partial x}+\nu\left(\frac{\partial^2 u}{\partial x^2}+\frac{\partial^2 u}{\partial y^2}\right) \tag{9}$$

$$u\frac{\partial v}{\partial x}+v\frac{\partial v}{\partial y}=-\frac{1}{\rho}\frac{\partial p}{\partial y}+\nu\left(\frac{\partial^2 v}{\partial x^2}+\frac{\partial^2 v}{\partial y^2}\right)+g\beta\Delta T \tag{10}$$

$$u\frac{\partial T}{\partial x}+v\frac{\partial T}{\partial y}=\alpha\left(\frac{\partial^2 T}{\partial x^2}+\frac{\partial^2 T}{\partial y^2}\right) \tag{11}$$

with $\Delta T = T - T_o$.

In the open cavity, the components of the gradient of a quantity along the x and y directions are of order of magnitude of the quantity multiplied to L^{-1} and b^{-1}, respectively. Following the analysis given by Bejan [27, Chapter 5, pp. 244–248, pp. 258–261 and problem 5.6, p. 303], deriving Eq. (9) with respect to y and Eq. (10) with respect to x and subtracting Eq. (9) from Eq. (10) is obtained

$$\frac{\partial u}{\partial x}\frac{\partial v}{\partial x}+u\frac{\partial^2 v}{\partial x^2}+\frac{\partial v}{\partial x}\frac{\partial v}{\partial y}+v\frac{\partial^2 v}{\partial x\partial y}-\frac{\partial u}{\partial y}\frac{\partial u}{\partial x}-\frac{\partial v}{\partial y}\frac{\partial u}{\partial x}+v\frac{\partial^2 u}{\partial y^2}$$
$$=\nu\left(\frac{\partial^3 v}{\partial x^3}+\frac{\partial^3 v}{\partial x\partial y^2}-\frac{\partial^3 u}{\partial y\partial x^2}-\frac{\partial^3 u}{\partial y^3}\right)+g\beta\frac{\partial T}{\partial x} \tag{12}$$

by Eq. (8), with δ the boundary layer thickness and l_p the penetration length

$$\frac{u}{l_p}\sim\frac{v}{\delta}\Rightarrow v\sim u\frac{\delta}{l_p} \tag{13}$$

for $l_p \gg \delta$ it is $v \ll u$ and the terms with highest order of magnitude are, by Eq. (12)

$$\frac{u^2}{l_p\delta}\quad \text{inertia} \tag{14}$$

$$\frac{\nu u}{\delta^3}\quad \text{friction} \tag{15}$$

$$\frac{g\beta\Delta T}{l_p}\quad \text{buoyancy} \tag{16}$$

for the considered thermal boundary condition, the temperature rise is $\Delta T \sim q\delta/k$ and hence the buoyancy is $g\beta q\delta/(kl_p)$

$$\text{buoyancy}\sim\text{friction}\Rightarrow\frac{\nu u}{\delta^3}\sim\frac{g\beta q\delta}{l_p k} \tag{17}$$

then

$$u\sim\frac{g\beta}{\nu}\frac{q\delta^4}{l_p k} \tag{18}$$

From Eq. (11)

$$u\frac{\Delta T}{l_p}\sim\alpha\frac{\Delta T}{l_p^2},\quad \alpha\frac{\Delta T}{\delta^2}\Rightarrow u\sim\alpha\frac{l_p}{\delta^2} \tag{19}$$

From Eq. (18)

$$\alpha\frac{l_p}{\delta^2}\sim\frac{g\beta}{\nu}\frac{q\delta^4}{l_p k} \tag{20}$$

Then

$$l_p\sim\delta Ra_\delta^{1/2} \tag{21}$$

For $\delta \sim b$

$$l_p\sim bRa^{1/2} \tag{22}$$

Or for $\delta \sim b/2$

$$l_p\sim 0.177bRa^{1/2} \tag{23}$$

It is worth noticing that Eq. (23) is in agreement with Bejan [27, problem 5.6, p. 303;5].

Fig. 11 shows the three possible fluid motion configurations inside the open-ended cavity: *full penetration* in an open-ended cavity with large aspect ratio b/L, in Fig. 11a, *from partial to full penetration*, in Fig. 11b, and *lateral penetration*, as suggested by Bejan and Kimura [5], in Fig. 11c. The choice of δ magnitude in terms of b is very important. This choice can be made depending on cavity aspect ratio. In fact, two limit conditions can succeed: $b/L \gg 1$, Fig. 11a, the distance between cavity horizontal walls is far greater than walls length; $b/L \ll 1$, Fig. 11c, the distance between cavity horizontal walls is much lower than walls length. Furthermore, a third configuration is possible: $b \sim L$, the channel height is of the same order of magnitude of the walls length. It can estimated that in the first case $\delta \ll b$, in the second case $\delta \sim b/2$ and in the third case $\delta < b/2$. The comparison between the penetration length l_p, which is experimentally evaluated by visualization and its estimation, which is obtained by Eq. (21) with $\delta = \zeta b$ and $l_p/b = \zeta^3 Ra^{1/2}$, is reported in Table 2 for several values of δ as a function of b. Note that for $b/2$, the estimation gives higher values than experimental results. Furthermore, this table shows that l_p depends on the estimation of boundary layer thickness. For the highest L/b values ($=10$), a good estimation of l_p is obtained with $\delta = (2/5)b$

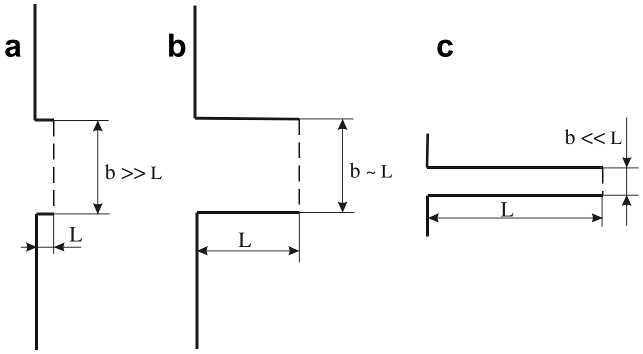

Fig. 11. Open-ended cavity geometries: (a) large aspect ratio; (b) aspect ratio with unitary order of magnitude; (c) small aspect ratio.

Table 2
Penetration length

L/b	Ra	l_p (mm)	l_p/b experimental	$l_p/b = \zeta^3 Ra^{1/2}$ with $\zeta = \delta/b$				
				$\delta = (1/2)b$	$\delta = (2/5)b$	$\delta = (1/3)b$	$\delta = (2/7)b$	$\delta = (1/4)b$
10	4.90×10^3	100	5	12.4	4.48	2.59	1.63	1.09
10	1.26×10^4	130	6.5	19.9	7.18	4.15	2.62	1.75
6.2	3.52×10^4	150	4.65	33.2	12.0	6.94	4.37	2.92
5	8.67×10^4	180	4.5	52.1	18.8	10.9	6.87	4.59

whereas for $(L/b) < 6.2$ a good estimation of l_p is obtained with $\delta = (1/4)b$ when $(L/b) = 5$, and $\delta = (2/7)b$ when $(L/b) = 6.2$. Some differences are observed with respect to the results given by Bejan and Kimura [5] due to the different heat transfer boundary condition on the horizontal wall and the aspect ratio.

4.3. Average Nusselt numbers and maximum wall temperatures correlations

The average Nusselt number, the maximum dimensionless wall temperature and the corresponding Grashof or Rayleigh number were determined by means of the experimental results using Eqs. (5), (2) and (1), respectively. Monomial correlations between Nu and Ra as well as between $T^+_{w,max}$ and Ra were obtained. The proposed correlations are:

$$Nu = 0.288\left(Ra\frac{b}{2L}\right)^{0.186} \tag{24}$$

with $r^2 = 0.988$, in the range $2.78 \times 10^3 < Ra < 3.90 \times 10^5$

$$T^+_{w,max} = 4.66\left(Ra\frac{b}{2L}\right)^{-0.203} \tag{25}$$

with $r^2 = 0.973$.

The correlations and the related experimental data for Eqs. (24) and (25) are reported in Fig. 12a and b, respectively. Both correlations show a very good relationship between the experimental data and the proposed relationships.

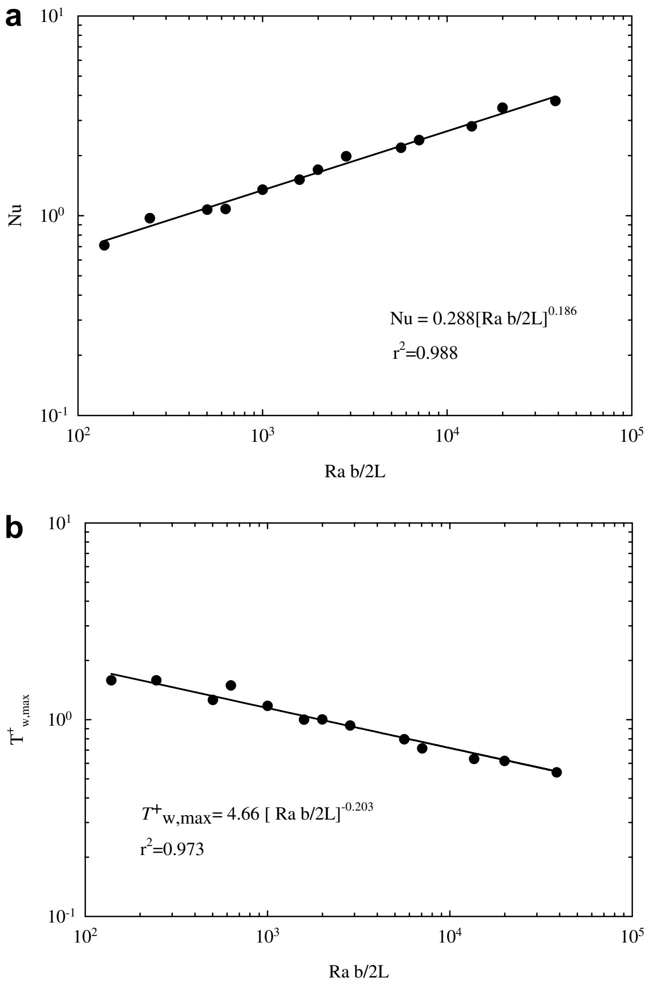

Fig. 12. Correlations between (a) average Nusselt number and Rayleigh number, (b) maximum dimensionless wall temperature and Rayleigh number.

5. Conclusions

An experimental investigation was carried out to obtain a phenomenological description of the air natural convection inside a horizontal open-ended cavity with heated upper plate and unheated lower plate. Smoke visualization and air temperature measurements were employed to analyze the fluid motion. Heat transfer characteristics of the heated wall were evaluated by the surface temperature measurements.

The results showed that, the flow inside the cavity was laminar and the penetration length depended on the Grashof number and particularly on the distance between the two horizontal plates. The pictures of the flow visualization showed that the fluid penetrated into the cavity, flowing along the lower plate, reversed its motion, close to the central region, and exited the cavity close to the upper plate in accordance with the results for the isothermally heated walls presented in [5], for water inside an open cavity, and in [1,13–16,20], for air inside an open ended cavity. The higher the Grashof number, the larger the penetration length. Finally, flow visualization showed a good agreement with streamlines fields given in [1,18], even if the configurations examined in these works had different boundary conditions, assigned temperature on lower and upper walls and higher than ambient temperature, and aspect ratio L/b lower than those studied in this work. The air temperature profiles inside the open-ended cavity confirmed the flow visualization observations. They showed that the temperature gradients along the gap cavity are weak for low heat fluxes values. The smaller the Grashof number the greater the diffusive effects. Scale analysis was carried out and showed that penetration length depends on $Ra^{1/2}$, in accordance with [5]. Furthermore, the estimation of the penetration length depended on the values of the boundary layer thickness evaluated in terms of distance between the walls. Correlations between average Nusselt number and Rayleigh number were proposed for $2.78 \times 10^3 < Ra < 3.90 \times 10^5$ and $10 \leqslant 2L/b \leqslant 20$. They fit the experimental results well.

Acknowledgements

This study was supported by the MIUR with a 2005 PRIN grant research program.

References

[1] K. Vafai, J. Ettefagh, The effects of sharp corners on buoyancy-driven flows with particular emphasis on outer boundaries, Int. J. Heat Mass Transfer 33 (10) (1990) 2311–2328.

[2] K. Vafai, C.P. Desai, S.V. Iyer, M.P. Dyko, Buoyancy induced convection in a narrow open-ended annulus, J. Heat Transfer 119 (1997) 483–494.

[3] M.M. Elsayed, W. Chakroun, Effect of aperture geometry on heat transfer in tilted partially open cavities, J. Heat Transfer 121 (1999) 819–827.

[4] M.M. Elsayed, N.M. Al-Najem, M.M. El-Refaee, A.A. Noor, Numerical study of natural convection in fully open tilted cavities, Heat Transfer Eng. 20 (3) (1999) 73–85.

[5] A. Bejan, S. Kimura, Penetration of free convection into a lateral cavity, J. Fluid Mech. 103 (1981) 465–478.

[6] O. LeQuere, J.A.C. Humphery, F.S. Sherman, Numerical calculation of thermally driven two-dimensional unsteady laminar flow in cavities of rectangular cross-section, Numer. Heat Transfer 4 (1981) 249–283.

[7] F. Penot, Numerical calculation of two-dimensional natural convection in isothermal open cavities, Numer. Heat Transfer 5 (1982) 421–437.

[8] C.F. Hess, R.H. Henze, Experimental investigation of natural convection losses from open cavities, J. Heat Transfer 106 (1984) 333–338.

[9] Y.L. Chan, C.L. Tien, A numerical study of two-dimensional natural convection in square open cavities, Numer. Heat Transfer 8 (1985) 65–80.

[10] Y.L. Chan, C.L. Tien, A numerical study of two-dimensional natural convection in shallow open cavities, Int. J. Heat Mass Transfer 28 (1985) 603–612.

[11] Y.L. Chan, C.L. Tien, Laminar natural convection in shallow open cavities, J. Heat Transfer 108 (1986) 305–309.

[12] A.H. Abib, Y. Jaluria, Penetrative convection in a stably stratified enclosure, Int. J. Heat Mass Transfer 38 (1995) 2489–2500.

[13] K. Vafai, J. Ettefagh, Thermal and fluid flow instabilities in buoyancy-driven flows in open-ended cavities, Int. J. Heat Mass Transfer 33 (10) (1990) 2329–2344.

[14] O. Manca, B. Morrone, S. Nardini, Visualization of flow structures in natural convection between horizontal heated parallel plates, J. Flow Visual. Image Proc. 7 (2000) 159–171.

[15] O. Manca, B. Morrone, S. Nardini, Experimental analysis of thermal instability in natural convection between horizontal parallel plates uniformly heated, J. Heat Transfer 122 (1) (2000) 50–57.

[16] A. Andreozzi, O. Manca, B. Morrone, Numerical analysis of air natural convection in open ended cavity uniformly heated from the upper plate, in: Proceedings of the 2001 ASME National Heat Transfer Conference, paper no. NHTC01-121310, Anaheim, California, USA, June 10–12, 2001.

[17] K. Khanafer, K. Vafai, Buoyancy-driven flows and heat transfer in open-ended enclosures: elimination of the extended boundaries, Int. J. Heat Mass Transfer 43 (2000) 4087–4100.

[18] K. Khanafer, K. Vafai, Effective boundary conditions for buoyancy-driven flows and heat transfer in fully open-ended two-dimensional enclosure, Int. J. Heat Mass Transfer 45 (2002) 2527–2538.

[19] S. Baskaya, H. Kauli, Effects of plate separation, plate length and temperature difference on buoyancy driven heat transfer in finite horizontal parallel plates, Heat Mass Transfer 40 (2004) 293–330.

[20] A. Andreozzi, Y. Jaluria, O. Manca, Numerical investigation on transient natural convection in a horizontal channel heated from upper wall, Numer. Heat Transfer A (2006) in press.

[21] T. Icoz, Y. Jaluria, Numerical simulation of boundary conditions and the onset of instability in natural convection due to protruding thermal sources in an open rectangular channel, Numer. Heat Transfer A 48 (2005) 831–847.

[22] W.K.S. Chiu, C.J. Richards, Y. Jaluria, Flow structure and heat transfer in a horizontal converging channel heated from below, Phys. Fluids 12 (8) (2000) 2128–2136.

[23] M.C. Chyu, On the boundary condition and data reduction of heat transfer experiment, Int. Commun. Heat Mass Transfer 14 (1987) 543–550.

[24] F.P. Incropera, D.P. DeWitte, Fundamentals of Heat and Mass Transfer, fourth ed., Wiley, New York, 1996.

[25] S.J. Kline, F.A. McClintock, Describing uncertainty in single sample experiments, Mech. Eng. 75 (1953) 3–12.

[26] R.J. Moffat, Describing the uncertainties in experimental results, Exp. Therm. Fluid Sci. 1 (1988) 3–17.

[27] A. Bejan, Convection Heat Transfer, third ed., Wiley, Hoboken, NJ, 2004.